Supplementary information for

Dynamical chiral high-harmonic generation via sub-cycle symmetry engineering

Hanqing Xu[1,*], Ying Ma[1,*], Jingyuan Niu[1], Yang Jiang[1,2], Wenyang Zheng[3],

Shuo Wang[3], Ya Bai[1,2,†], Candong Liu[1,2,†], Peng Liu[1,3,†], Ruxin Li[1,2,3,†]

[1] *State Key Laboratory of Ultra-intense Laser Science and Technology, Shanghai Institute of Optics and Fine Mechanics, Chinese Academy of Sciences, Shanghai, 201800, China.*

[2] *Center of Materials Science and Optoelectronics Engineering, University of Chinese Academy of Sciences, Beijing, 100049, China.*

[3] *Zhangjiang Laboratory, Shanghai 201210, China.*

[*] *These authors contributed equally to this work.*

[†] *Corresponding author*: pipbear@siom.ac.cn; cdliu@siom.ac.cn; peng@siom.ac.cn; ruxinli@siom.ac.cn

I. Experimental Details

1.1 Experimental Setup

The mid-infrared laser and high-harmonic generation (HHG) measurements are shown in Figure S1(a). We use laser pulses at a fundamental photon energy of 326 meV (3800 nm) from a home-built dual-optical parametric amplifiers (DOPA). Two-color driving pulses are created via frequency doubling in an AGS crystal (Dien Tech, type-I, 400 μm-thick) for second-harmonic generation (SHG). An in-line phase compensator, composed of a ZnS plate, a pair of BaF_2 wedge, a dual-wavelength quarter-waveplate (DWP) and a nanoparticle linear film polarizer providing stable phase locking, is deployed for precise two-color phase delay control. To monitor the phase delay between the fundamental and second-harmonic (SH) fields, an interference technique is employed, passing the two-color pulse into a 100 μm-thick GaSe crystal. The interferometric fringes between the newly generated SH pulse in GaSe and the existing SH field are recorded, establishing the reference for the two-color field's relative phase shift in each measurement.

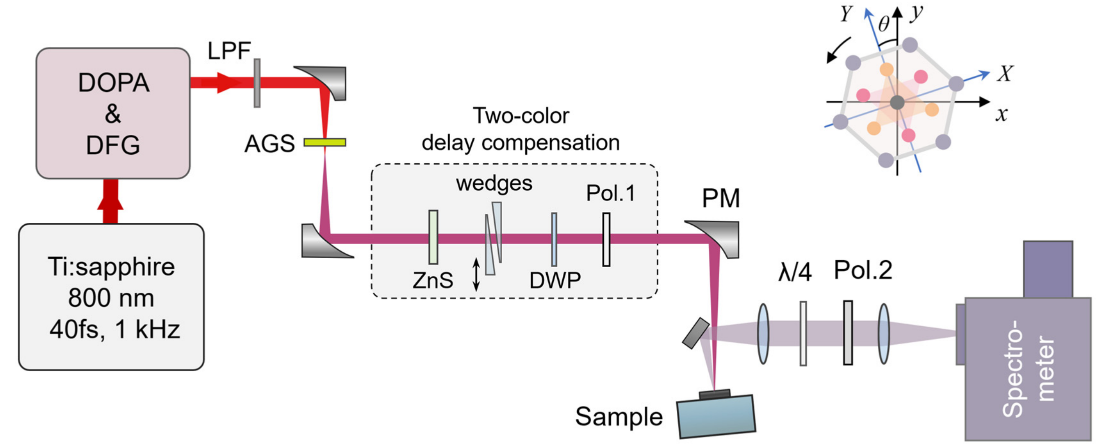

Figure S1. Experimental layout for the HHG polarization control and measurement. Upper right inset: Relationship between the laboratory coordinate (*x*-*y* plane) and the crystal coordinate (*X*-*Y* plane). The intersection line of the mirror symmetry plane and the crystal surface is along the *Y*-axis direction.

High-harmonics are generated by focusing the two-color field onto the sample (Bi_2Se_3, BiTeI) surface at an angle of incidence about 5°, with a peak field of 5.2 MV

cm^{-1}. The harmonic emission is detected by a grating spectrometer with a thermoelectrically cooled CCD camera. Both the fundamental and SH fields have independently controllable intensity and precisely tunable phase delay. In the experiments the SH field acts as a perturbation, the relative power of which is 10^{-4} to 10^{-3} times that of the fundamental pulse.

1.2 Stokes polarimetry measurement

To measure the polarization state of the emitted harmonics, a polarimetry setup consisting of a rotating achromatic quarter-wave plate (QWP) and a fixed a superbroadband wired grid polarizer (transmission axis along the *y* direction) were used. The intensity of the harmonics is measured as a function of the rotation angle of the QWP (β), the Stokes parameters S_0,S_1,S_2 and S_3 can be calculated, providing a comprehensive description of the polarization state of HHG.

The detected intensity $I(\beta)$ is derived from the Stokes parameters of the input beam and expressed as

$$I(\beta)=\frac{1}{2}(S_0+S_1\cos^2 2\beta+S_2\cos 2\beta\sin 2\beta+S_3\sin 2\beta). \tag{1.1}$$

This equation is further reformulated into a truncated Fourier series

$$I(\beta)=\frac{1}{2}(A+B\sin 2\beta+C\cos 4\beta+D\sin 4\beta), \tag{1.2}$$

where the coefficients A, B, C, and D relate to the Stokes parameters as

$$A=S_0+\frac{S_1}{2},\quad B=S_3,\quad C=\frac{S_1}{2},\quad D=\frac{S_2}{2}. \tag{1.3}$$

To resolve the harmonic components, intensity measurements are taken at $N=8$ equally spaced angular positions over a 180° rotation of the waveplate, as dictated by Nyquist's sampling theorem. The discrete intensities I_n at angles $\beta_n=\frac{n}{N}180^\circ$ $(n=1,2,\ldots,N)$ are recorded. The Fourier coefficients take the form of

$$A=\frac{2}{N}\sum_{n=1}^{N}I_n,\ B=\frac{4}{N}\sum_{n=1}^{N}I_n\sin 2\theta_n,\ C=\frac{4}{N}\sum_{n=1}^{N}I_n\cos 4\theta_n,\ D=\frac{4}{N}\sum_{n=1}^{N}I_n\sin 4\theta_n. \tag{1.4}$$

Finally, the Stokes parameters are extracted from the coefficients

$$S_0=A-C,\quad S_1=2C,\quad S_2=2D,\quad S_3=B. \tag{1.5}$$

The polarization state of HHG, that is the orientation angle Ψ and the ellipticity angle χ, can be calculated from the measured Stokes parameters

$$\begin{cases} \Psi = \frac{1}{2}\mathrm{atan}\left(\frac{S_2}{S_1}\right) \\ \chi = \frac{1}{2}\mathrm{atan}\left(\frac{S_3}{\sqrt{S_1^2 + S_2^2}}\right) \end{cases}. \tag{1.6}$$

The orientation angle Ψ indicates the rotation of the polarization ellipse relative to the reference axis, while the ellipticity angle χ describes the ratio of the minor axis to the major axis of the polarization ellipse. By analyzing these parameters, we can gain insights into the polarization modulation of the HHG radiation.

1.3 Samples

The Bi_2Se_3 crystals were synthesized via the self-flux method by precisely controlling the stoichiometric ratio of high-purity Bi and Se in a sealed silica ampoule. Excess Se was added to suppress the Se vacancy formation in the crystal bulk and to improve the crystal quality. BiTeI single crystals were grown by chemical vapor transport. Polycrystalline BiTeI was first synthesized by annealing stoichiometric Bi, Te, and I in an evacuated quartz ampule. The resulting powder was mixed with I_2 transport agent, and subjected to a thermal gradient in a two-zone furnace. High-quality layered BiTeI crystals were grown after controlled cooling. Both samples were provided by Muke-nano Tech. In HHG experiments, single crystals size of about 2 mm with optically flat surface along the (111) direction is obtained by mechanical exfoliation.

The GaSe crystal, with a thickness of 30 μm and a cleavage plane (z-cut), was mounted in a one-inch holder. In the HHG experiment, the transmission geometry was employed, where midinfrared pulse were focused onto the crystal and HHG was measured in the transmission direction.

1.4 Flexible wavelength scalability for polarization control

In this section, we demonstrate that the polarization section has versatile compatibility with diverse materials and spectral regimes. Figure S2b shows the typical HHG spectrum measured from BiTeI. BiTeI is a non-centrosymmetric material that belongs to the trigonal space group (P3m1) with symmetry operation C_{3v} and exhibits a giant Rashba-type spin splitting in its band structure[1]. The intrinsic bulk inversion symmetry breaking in BiTeI facilitates the generation of even-order harmonics (H4-H8, Fig. S2), which are controllable under the proposed two-color driven harmonic polarization control scheme.

Harmonics ranging from H4 to H8 can all be dynamically modulated in the presence of SH field, as shown in Fig. S5. As the SH field increases, the ellipticity angle modulation gradually increases to an optimum value and then decreases. During this process, the polarization direction switches from perpendicular to the driving light to parallel polarization. Notably, H4 and H8 achieve full polarization control almost simultaneously at the driving field strengths of F_{ω} = 5.2 MV cm^{-1} and $F_{2\omega}$ = 200 kV cm^{-1} (Fig. S6a), while H6 requires a higher SH field ($F_{2\omega}$ = 275 kV cm^{-1}, Fig. S6b). The evolution of the polarization ellipse for these harmonics is depicted in Fig. S6c-d, demonstrating quarter-wave plate-like behavior through the tuning of the relative phase of the driving fields. This ability to control multi-order harmonics control highlights the broadband spectral applicability of the present scheme, which holds significant potential for multi-color spectroscopy and coherent control applications. The observed asynchronous polarization modulation can be attributed to interband Berry phase-induced spectral shifts[2], where the electron-hole quasiparticles accumulate geometric phases along their evolution paths. This asynchronous modulation effect provides a unique capability to decouple harmonic responses, enabling diverse polarization control strategies through spectral selectivity.

1.5 Polarization manipulation in the near-ultraviolet region

In this section we show the full polarization manipulation of HHG in the near-ultraviolet region. This is achieved in the ε-GaSe crystal, space group $P6_3/mmc$ with symmetry operation C_{6v}. The high-harmonic spectrum from GaSe can extend up to the

11th order. As shown in Fig. S7 for the 10th harmonic (H10, photon energy 3.16 eV). Notably, synchronized ellipticity tuning across the entire spectral range enables full polarization modulation within an ellipticity range of ±1, spanning from left-handed circular polarization through linear polarization to right-handed circular polarization (see Fig. 5d-f in the main text).

Importantly, by employing near-infrared bichromatic laser fields (e.g., 800 + 400 nm) combined with wide-bandgap crystals such as SiO_2 or hBN, complete polarization control can be extended to the vacuum ultraviolet (VUV) and even the extreme ultraviolet (EUV) regimes. This approach leverages the enhanced nonlinear susceptibility and phase-matching conditions in engineered materials, opening avenues for attosecond polarization shaping in high photon energy spectral regions.

1.6 Supplementary experimental figures

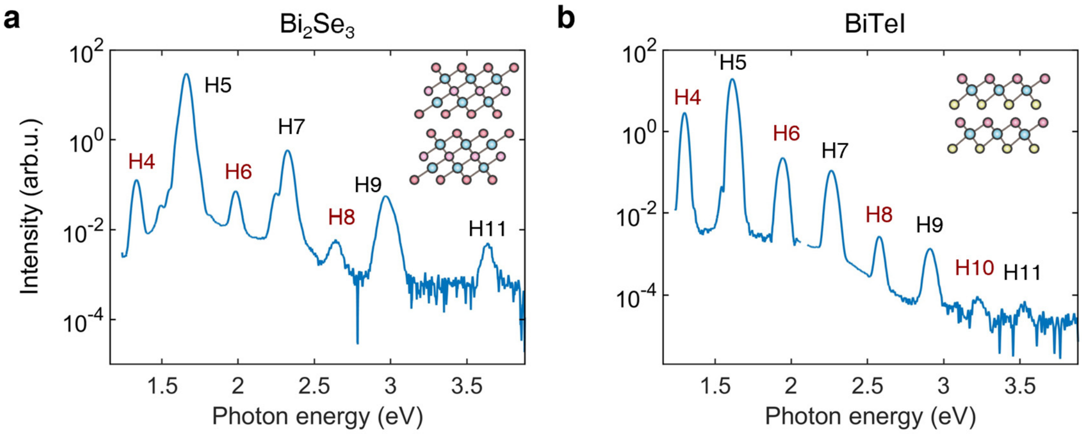

Figure S2: High-harmonic spectra of Bi_2Se_3 (a) and BiTeI (b) samples driven by the fundamental pulse. The driving pulse intensities in the two cases are F_ω = 5.2 MV cm^{-1} and 4.7 MV cm^{-1}, respectively, polarized along the $\overline{\Gamma} - \overline{\mathrm{K}}$ direction.

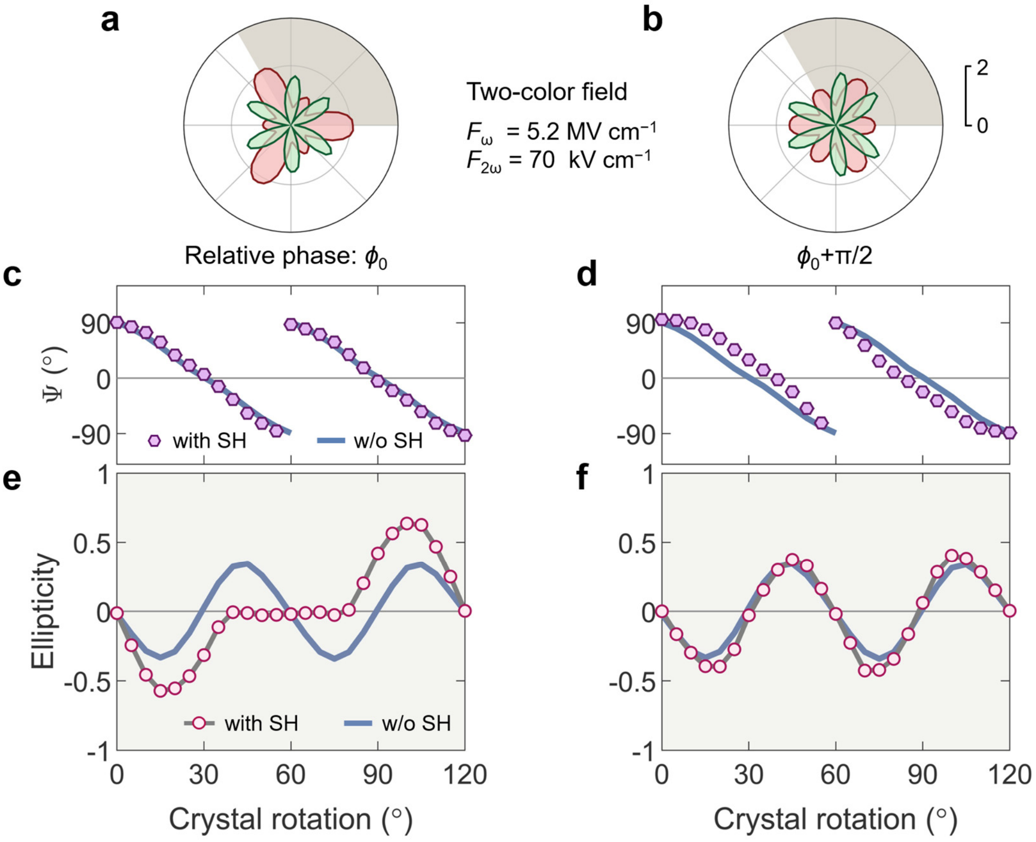

Figure S3. Modulation of HHG via broken dynamical symmetry for SH field of 70 kV cm^{-1}. a,**b**, Azimuthal rotation dependence of H6 yield measured under parallel (red curve) and perpendicular (blue curve) polarization configurations. The results show two group data with a relative phase difference of π/2. **c**,**d**, Orientation angle (Ψ) of the harmonic polarization ellipse as a function of crystal azimuth angle. The crystal rotation angle-dependent Ψ modulated by a weak SH field is represented by purple hexagons, whereas Ψ in the absence of the SH field is depicted as green lines. **e**,**f**, Measured ellipticity of the harmonic polarization. The crystal rotation angle-dependent ellipticity modulated by a weak SH field is represented by purple hexagons, whereas ellipticity in the absence of the SH field is depicted as green lines.

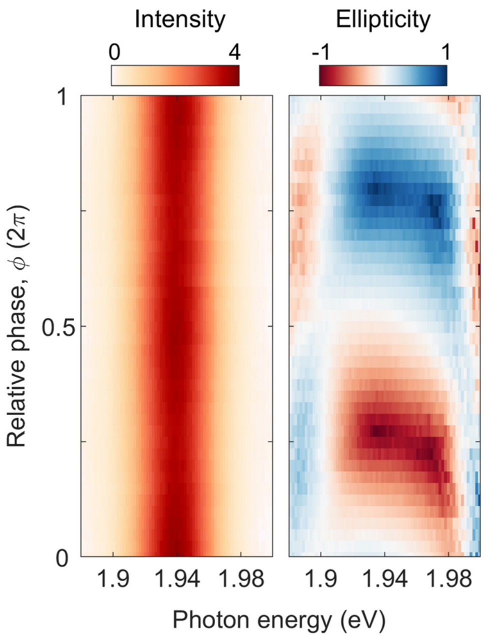

Figure S4. Spectral-resolved full polarization manipulation of HHG from Bi_2Se_3. Modulation of the spectral intensity (left), ellipticity (right) from Bi_2Se_3 (90°) versus the relative phase offset, shows broadband polarization state control across the harmonic spectra.

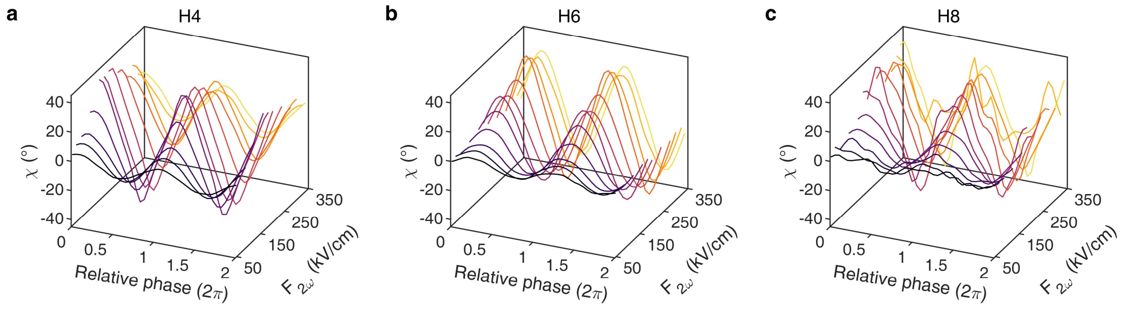

Figure S5. Modulation of the ellipticity angle under the control of relative phase and SH field strength. The results were measured from BiTeI. Upon increasing the SH field strength, the modulation depth initially grows, attains a maximum value, and subsequently decrease. The characteristic modulation peak unambiguously determines the optimal SH field strength ($F_{2\omega}$) for achieving complete polarization control, while exhibiting systematic variation across even harmonic orders

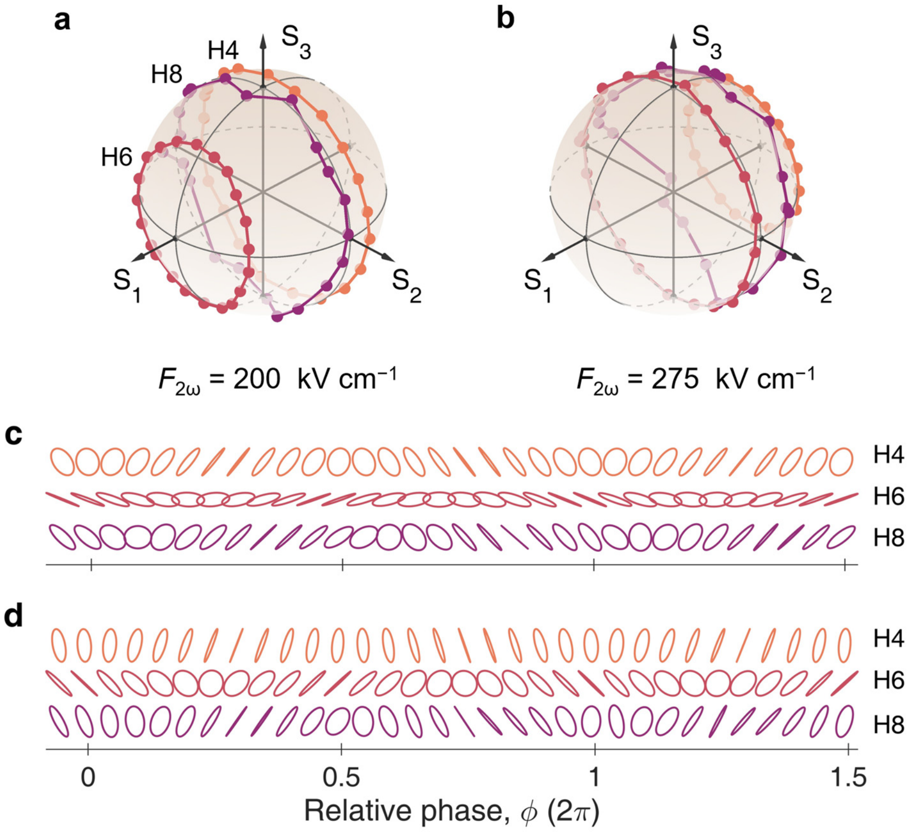

Figure S6. Dependence of the polarization conversion on the harmonic orders measured in BTI. **a**,**b**, Evolution of the polarization state trajectories for three harmonic orders, H4 (yellow dots and line), H6 (red dots and line), and H8 (purple dots and line). SH field of 200 kV cm^{-1} and 275 kV cm^{-1} are adopted in **a** and **b**, respectively. **c**,**d**, Map of the polarization ellipse as a function of relative phase for varying harmonic orders. The color codes are the same as in panels **a** and **b**. Quarter-wave plate (HWP) like operation is observed for H4 and H8 when $F_{2\omega}$ = 200 kV cm^{-1}, and for H6 when $F_{2\omega}$ = 275 kV cm^{-1}.

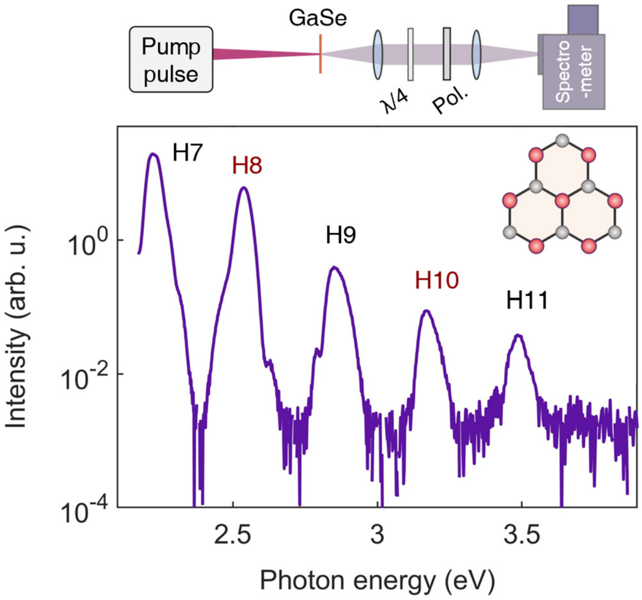

Figure S7. High-harmonic spectra of the GaSe sample driven by the fundamental pulse. The driving pulse, with an intensity of F_ω = 6.5 MV cm^{-1} at center wavelength of 3900 nm, is polarized along the $\bar{\Gamma}-\bar{K}$ direction. Harmonics up to H11 is observed, with the spectrum extends to near-ultraviolet region (photon energy: 3.1~4.13 eV). Upper inset: schematic diagram of the transmissive harmonic measurement setup. Inner inset: the top view of the GaSe crystal structure.

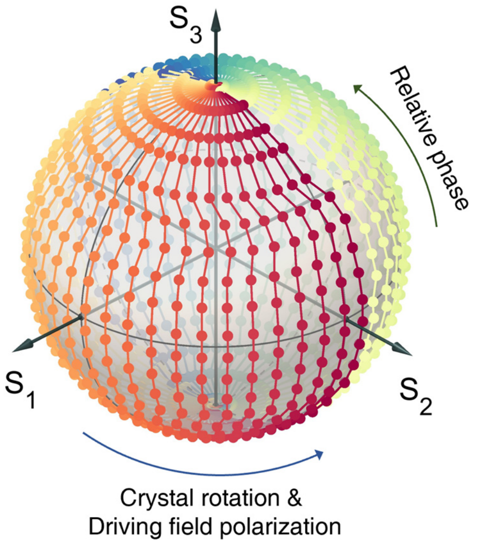

Figure S8. Illustration of full Poincaré sphere polarization state control. This can be achieved through the combined adjustment of two-color relative phase, driving field polarization, and crystal angular rotation.

II. Model for simulation

2.1. Nonperturbative currents

We simulate the HHG polarization control by solving the semiconductor Bloch equations (SBEs). The harmonic response in topological insulator surface states is calculated to elucidate the underlying mechanism of polarization-modulated harmonic generation. The formalism employs the surface state Hamiltonian and SBEs framework detailed in Refs. [2,3], with full mathematical implementation provided therein.

Our analysis focuses on the non-perturbative currents driven by the strong light field, with comprehensive derivations of the current expression are present in the following section. The interband J_{er}^{j} and intraband J_{ra}^{j} components of the microscopic current are derived as:

$$J_{\mathrm{er}}^{j}(t) = -\int_{\mathrm{BZ}} d^2\boldsymbol{k}\, \mathcal{E}_g(\boldsymbol{k})\, |d_{cv}^{j}(\boldsymbol{k})| \int_{-\infty}^{t} |F(t')\, d_{cv}^{y}[\boldsymbol{\kappa}(t,t')]|\, e^{-iS(t',t,\mathbf{k})-(t-t')/T_2}\, dt' + \text{c.c.}, \tag{2.1}$$

$$\begin{aligned} J_{\mathrm{ra}}^{j}(t) = \int_{\mathrm{BZ}} d^2\boldsymbol{k}\, \mathcal{E}_g(\boldsymbol{k})\, |\boldsymbol{d}_{cv}^{j}(\boldsymbol{k})| \int_{-\infty}^{t} dt' \int_{-\infty}^{t'} dt'' |F(t')\, d_{cv}^{y}[\boldsymbol{\kappa}(t,t')]| \\ |F(t'')\, d_{cv}^{y}[\boldsymbol{\kappa}(t'',t')]|\, e^{-iS(t'',t',\mathbf{k})-(t-t')/T_2} + \text{c.c.}, \end{aligned} \tag{2.2}$$

where $\mathcal{E}_g(\boldsymbol{k})$ denotes the crystal momentum-dependent bandgap, $v_{\mathrm{m}}(\boldsymbol{k}) = \nabla_{\boldsymbol{k}} \mathcal{E}_{\mathrm{m}}(\boldsymbol{k})$ represents the group velocity of electron wavepackets, $d_{cv}^{j}(\mathbf{k})$ is the transition dipole matrix element describing polarization of electron-hole (e-h) pairs, and T_2 is the dephasing time of the coherence. The time-dependent crystal momentum is given by $\boldsymbol{\kappa}(t',t) = \boldsymbol{k} + \boldsymbol{A}_{\mathrm{p}}(t') - \boldsymbol{A}_{\mathrm{p}}(t)$, where $\boldsymbol{A}_{\mathrm{p}}(t) = -\int_{-\infty}^{t} \boldsymbol{F}_{\mathrm{p}}(\tau)\, d\tau$ corresponds to the vector potential of the pump field $\boldsymbol{F}_{\mathrm{p}}(t)$. High-harmonic emission can therefore be obtained by Fourier transforming the total current $\boldsymbol{J}_{\mathrm{tot}}(t) = \boldsymbol{J}_{\mathrm{ra}}(t) + \boldsymbol{J}_{\mathrm{er}}(t)$ under the electric dipole approximation, $\boldsymbol{E}_{\mathrm{HH}}(N\omega) = iN\omega \int \boldsymbol{J}(t)\, e^{iN\omega t}$, N is an integer represents the harmonic order.

2.2. Semiclassical action and interband Berry phase

The semiclassical action $S(\boldsymbol{k},t',t)$, governing phase accumulation along e-h trajectories, comprises two terms: $S(\boldsymbol{k},t',t) = S_{\mathrm{dyn}}(\boldsymbol{k},t',t) + \gamma_{\mathrm{B}}(\boldsymbol{k},t',t)$, where S_{dyn} represents the dynamic phase and γ_{B} interband Berry phases. For a driving laser polarized along the *y*-axis, these phases are expressed as:

$$S_{\mathrm{dyn}}(\boldsymbol{k},t',t) = \int_{t'}^{t} E_{cv}[\boldsymbol{\kappa}(t,\tau)]\, d\tau, \tag{2.3}$$

$$\gamma_{\mathrm{B}}^{j}(\boldsymbol{k},t',t) = \int_{t'}^{t} \boldsymbol{F}(\tau)\Delta\boldsymbol{\mathcal{A}}[\boldsymbol{\kappa}(t,\tau)]\, d\tau + \alpha_{\mathrm{cv}}^{j}(\boldsymbol{k}) - \alpha_{\mathrm{cv}}^{y}[\boldsymbol{\kappa}(t,t')]. \tag{2.4}$$

Here, γ_{B}^{j} (for $j = x,y$) represents the interband Berry phase to include gauge-invariant contributions from band evolution and transition dipole phases. Recent experiments have observed such interband Berry phases in $\mathrm{SiO_2}$ crystals and topological surface states[2,4].

The Berry phase arises from the geometric structure of electronic wavefunctions, encoded in the transition dipole matrix elements[5-8]:

$$\boldsymbol{d}_{\mathrm{m'm}}(\boldsymbol{k}) = \langle u_{\mathrm{m'}}^{\boldsymbol{k}} | i\nabla_{\boldsymbol{k}} | u_{\mathrm{m}}^{\boldsymbol{k}} \rangle, \tag{2.5}$$

where $u_{\mathrm{m}}^{\boldsymbol{k}}$ is the periodic part of the Bloch wavefunction. The diagonal elements

$$\boldsymbol{\mathcal{A}}_{\mathrm{m}}(\boldsymbol{k}) = \boldsymbol{d}_{\mathrm{mm}}(\boldsymbol{k}) \tag{2.6}$$

define the Berry connection that describes the intraband quantum geometry. Off-diagonal elements $\mathrm{m'} \neq \mathrm{m}$ originate from diabatic interband transitions, with the transition dipole phase

$$\alpha(\boldsymbol{k}) = \arg[\boldsymbol{d}_{\mathrm{m'm}}(\boldsymbol{k})]. \tag{2.7}$$

Both the Berry connection and transition dipole phase are critical for the inter-half cycle spectral interference in high-harmonic emission.

2.3. Simulation results

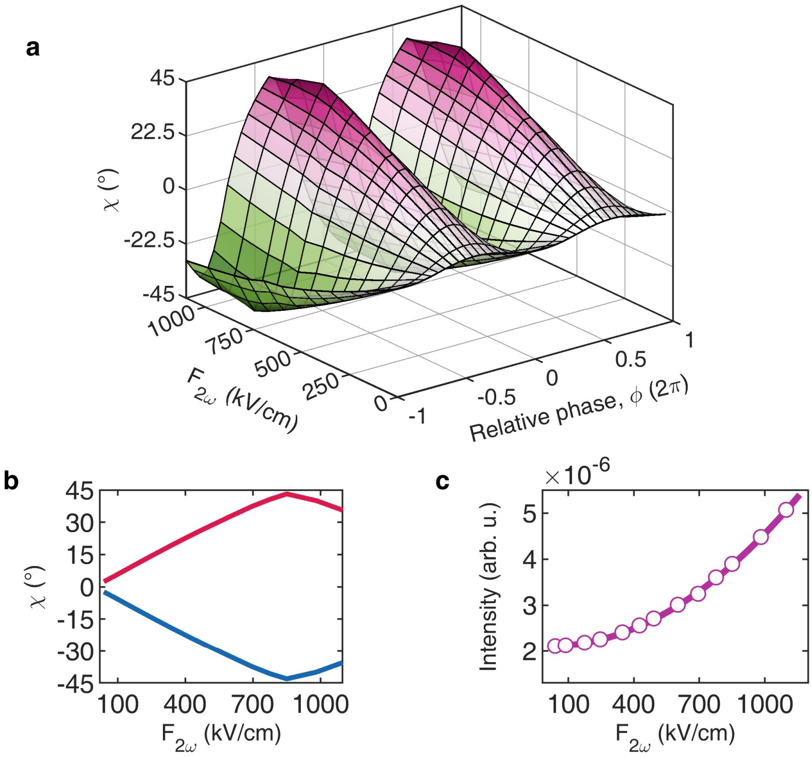

Figure S9. Tune the polarization selection rule with the asymmetric laser field. a, Harmonic ellipticity manipulation through the SH field strength and relative phase (fundamental field F_ω = 5.0 MV cm^{-1}). **b**, Maximum ellipticity versus SH field at phase values of −0.7π (red line) and 0.3π (blue line), extracted from **a**. **c**, Harmonic yield scaling shows quadratic dependence ($I_{\mathrm{HH}} \propto F_{2\omega}^2$) by fitting (purple line) the simulated data (purple circles). Notably, the simulation required about four times stronger SH fields compared to the experimental values, probably due to our tight-binding model overestimate the momentum-space expansion of the Bi_2Se_3 surface state. This phase-space extension of electron states requires stronger SH field to effectively perturb the electron-hole dynamics. Despite this quantitative mismatch, the simulated intensity scaling is in agreement with the perturbative approximation, as described by Eq. 3.20 in Section III.

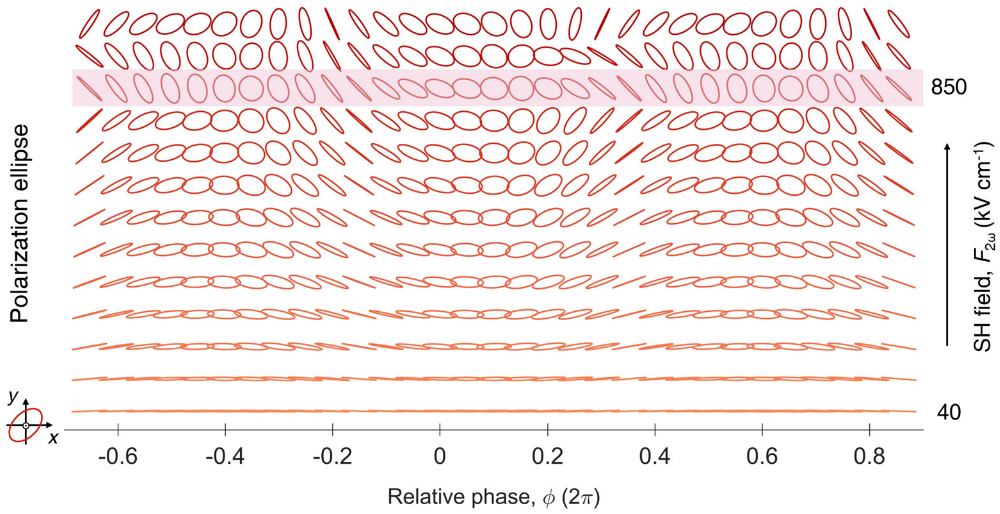

Figure S10. Polarization ellipse of H6 versus relative phase under increasing SH fields. Increasing the SH field strength increases the modulation extent of the harmonic ellipticity. Complete chiral and ellipticity modulation of H6 is achieved at $F_{2\omega}$ = 850 kV cm^{-1}. The ellipticity decreases with further increase of the SH field.

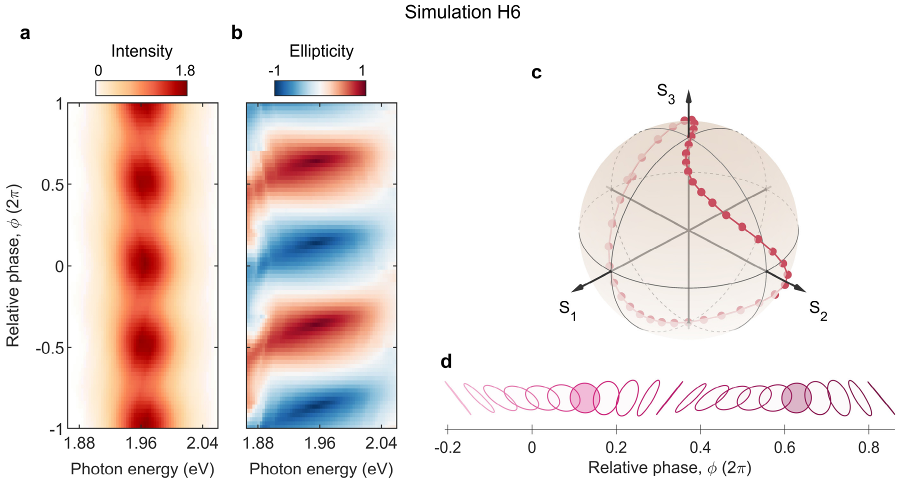

Figure S11. Simulated full-polarization manipulation of H6 from Bi_2Se_3. a,**b**, Modulation of the simulated spectral intensity (**a**) and ellipticity (**b**) by tunning the relative phase delay. The results show broadband polarization conversion across the harmonic spectrum. **c**, Trajectories of the polarization states on the normalized Poincaré sphere. Full controllability of the polarization is achieved with an azimuth orientation that depends slightly on the relative phase. **d**, Transformation of the polarization ellipse from linear to circular by precise drive field delay control.

III. Analytical expression under dynamical symmetry

3.1 Dynamical symmetry

Dynamical symmetry determines the selection rule of the light-matter interacting system, which simultaneously encompasses the spatial-temporal symmetries of the light field and the lattice structure[10-12]. The point group symmetry of the Bi_2Se_3 and BiTeI crystals is C_{3v}, which includes: a threefold rotation axis (C_3) along the c-axis direction and three vertical mirror planes passing through the c-axis at 120° intervals (see inset of Fig. S1). The linearly polarized pump laser pulse possesses time reversal symmetry and second-order time translation operations. By applying the mirror symmetry operation ($\hat{M}_X$), the time-reversal symmetry operation ($\hat{T}$), and the second-order time translation ($\hat{\tau}_2$), we can derive the analytical expression for HHG.

Practically, in the derivation process, we separately apply the time-domain symmetry and spatial symmetry operations in the derivation. For time-domain operation, we define an operator $\mathbb{T} \equiv \hat{T}\hat{\tau}_2$, with a single-color pump field $\boldsymbol{F}_{\rm p} = \boldsymbol{F}_{\omega}\cos(\omega t)$, with the vector potential given by $\boldsymbol{A}_{\rm p}(t) = \boldsymbol{A}_{\omega}\sin(\omega t)$ without loss of generality. The time-dependent quasimomentum and pump-field vector potentials transform as $\mathbb{T}\boldsymbol{k}(t) = -\boldsymbol{k}(t)$ and $\mathbb{T}\boldsymbol{A}_{\rm p}(t) = -\boldsymbol{A}_{\rm p}(t)$, respectively. Under the action of the temporal operator, the dynamic phase and the interband Berry phase are transformed as

$$\mathbb{T}S_{\rm dyn}(\boldsymbol{k},t,t')\mathbb{T}^{\dagger} = S_{\rm dyn}(-\boldsymbol{k},\hat{\tau}_2 t,\hat{\tau}_2 t') = S_{\rm dyn}(\boldsymbol{k},t,t'), \tag{3.1}$$

$$\mathbb{T}\gamma_{\rm B}^{j}(\boldsymbol{k},t',t))\mathbb{T}^{\dagger} = \gamma_{\rm B}^{j}(-\boldsymbol{k},\hat{\tau}_2 t,\hat{\tau}_2 t') = -\gamma_{\rm B}^{j}(\boldsymbol{k},t',t), \tag{3.2}$$

Here, $\gamma_{\rm B}^{j}(\boldsymbol{k},t',t)$ represent the interband Berry phase for parallel (*y*-axis) and orthogonal (*x*-axis) polarizations

$$\gamma_{\rm B}^{j}(\boldsymbol{k},t',t) = \int_{t'}^{t} \boldsymbol{F}(\tau)\Delta\boldsymbol{\mathcal{A}}[\boldsymbol{\kappa}(t,\tau)]\,d\tau + \alpha_{cv}^{j}(\boldsymbol{k}) - \alpha_{cv}^{y}[\boldsymbol{\kappa}(t,t')]. \tag{3.3}$$

Therefore, $\gamma_{\rm B}^{x}(t',t,\boldsymbol{k}) = \gamma_{\rm B}^{y}(t',t,\boldsymbol{k}) + \alpha_{\rm DP}(\boldsymbol{k})$, where $\alpha_{\rm DP}(\boldsymbol{k}) = \alpha_{cv}^{x}(\boldsymbol{k}) - \alpha_{cv}^{y}(\boldsymbol{k})$ quantifies the polarization-dependent phase difference.

For the even-order harmonics of primary interest here, the interband contribution dominates[2]. Therefore, in the following analytical analysis, we only need to consider the interband current term. The interband current operator exhibits the following transformation properties under $\mathbb{T}$ symmetry

$$\begin{aligned}\mathbb{T}J_{\mathrm{er}}^{j}(\boldsymbol{k},t',t)\mathbb{T}^{\dagger} &= J_{\mathrm{er}}^{j}(-\boldsymbol{k},\hat{\tau}_2 t',\hat{\tau}_2 t) \\ &= -J_{\mathrm{er}}^{j}(\boldsymbol{k},t',t)\,e^{2i\gamma_{\mathrm{B}}^{j}(\boldsymbol{k},t',t)}.\end{aligned} \tag{3.4}$$

Based on the time-domain symmetry operation, we derive the current components in the *x*-*y* coordinate (see Fig. S1), denoted as J_{er}^{x} and J_{er}^{y}. These current components are then projected onto the crystal coordinate system (*X*-*Y* coordinate) and subjected to the mirror operation $\hat{M}_X J_{\mathrm{cv}}^{X}\hat{M}_X^{\dagger} = -J_{\mathrm{cv}}^{X}$, $\hat{M}_X J_{\mathrm{cv}}^{Y}\hat{M}_X^{\dagger} = J_{\mathrm{cv}}^{Y}$. Finally, the analytical harmonic expression is obtained from the symmetry-modified currents.

3.2 Harmonic components of single-color pulse as the driver

Driven by a multicycle laser field, the high-harmonic response is the interference of a sequence of subcycle bursts emitted from recombination events in adjacent-half cycles. Therefore, the interband current is simplified to the coherent sum of subcycle resolved current surges

$$J_{\mathrm{er}}^{j}(N\omega)\propto\left(e^{-i\gamma_{\mathrm{B}}^{j}(\boldsymbol{k}_{+},t'_{+},t_{+})}-e^{-iN\pi}e^{i\gamma_{\mathrm{B}}^{j}(\boldsymbol{k}_{-},t'_{-},t_{-})}\right)\left|\boldsymbol{d}_{\mathrm{cv}}^{\boldsymbol{k}}\right|\left|\boldsymbol{d}_{\mathrm{cv}}^{\boldsymbol{\kappa}(t'_{+},t_{+})}\right|F(t'_{+})\,\mathrm{e}^{-iN\omega_0 t-iS_1(\boldsymbol{k}_{+},t'_{+},t_{+})}, \tag{3.5}$$

where *N* is an integer that represents the harmonic order, subindices +/– denote the variable in positive/negative half-cycles, respectively.

By projecting the interband current along the polarization axis and its orthogonal direction of the driving laser, the two harmonic current components can thus be represented by the following matrix form

$$\begin{pmatrix}J_{\mathrm{er}}^{x}\\ J_{\mathrm{er}}^{\mathrm{y}}\end{pmatrix}=g_{\boldsymbol{\kappa},0}\begin{pmatrix}\left(e^{-i\gamma_{\mathrm{B},x}^{+}}-e^{-iN\pi}\cdot e^{i\gamma_{\mathrm{B},x}^{-}}\right)\left|\boldsymbol{d}_{\mathrm{cv}}^{\boldsymbol{k},x}\right|\\ \left(e^{-i\gamma_{\mathrm{B},y}^{+}}-e^{-iN\pi}\cdot e^{i\gamma_{\mathrm{B},y}^{-}}\right)\left|\boldsymbol{d}_{\mathrm{cv}}^{\boldsymbol{k},y}\right|\end{pmatrix}e^{-i(N\omega_0 t-S_1)}, \tag{3.6}$$

here, $g_{\boldsymbol{\kappa},0} = |\boldsymbol{d}_{\mathrm{cv}}^{\boldsymbol{\kappa}(t',t)}| F(t')$, the geometric phase is acquired through optical field oscillations with opposite polarities, with the phases for the positive and negative half-cycles denoted as $S_{2,j}^{+}$ and $S_{2,j}^{-}$ respectively. It is known that the geometric phase significantly modulates the responses of Bloch electron in neighbor half-cycles of the optical field, result in distinct phase accumulation. Specifically, e-h pairs driven by the negative optical half-cycle exhibit prolonged trajectories and consequently higher recombination photon energies. To quantitatively characterize the accumulated geometric phase and transition dipole moment phase during half-cycle evolution, we define the cycle-averaged quantity $\bar{\gamma}_{\mathrm{B},j} = \frac{1}{2}(\gamma_{\mathrm{B},j}^{+} + \gamma_{\mathrm{B},j}^{-})$ and $\bar{\alpha}_{\mathrm{DP},j} = \frac{1}{2}(\alpha_{\mathrm{DP},j}^{+} + \alpha_{\mathrm{DP},j}^{-})$, here $\gamma_{\mathrm{B},j}^{\pm} = \bar{\gamma}_{\mathrm{B},j} \pm \Delta\gamma_{\mathrm{B},j}$, $\alpha_{\mathrm{DP},j}^{\pm} = \frac{1}{2}(\bar{\alpha}_j \pm \delta\alpha)$, $\Delta\gamma_B^j = \alpha_{cv}^j - \alpha_{cv}^y$, $\delta\alpha$ are all the deviations from the average value. According to Eq. (3.3) we can get $\gamma_{\mathrm{B},x}^{\pm} = \gamma_{\mathrm{B},y}^{\pm} + \alpha_{\mathrm{DP}}^{\pm}$, and rewrite

$$\begin{pmatrix} J_{\mathrm{er}}^{x} \\ J_{\mathrm{er}}^{\mathrm{y}} \end{pmatrix} = g_{\boldsymbol{\kappa},0} \begin{pmatrix} \left(e^{-i(\gamma_{\mathrm{B},y}^{+} + \alpha_{\mathrm{DP}}^{+})} - e^{-iN\pi} \cdot e^{i(\gamma_{\mathrm{B},y}^{-} + \alpha_{\mathrm{DP}}^{-})}\right) |\boldsymbol{d}_{\mathrm{cv}}^{\boldsymbol{k},x}| \\ \left(e^{-i\gamma_{\mathrm{B},y}^{+}} - e^{-iN\pi} \cdot e^{i\gamma_{\mathrm{B},y}^{-}}\right) |\boldsymbol{d}_{\mathrm{cv}}^{\boldsymbol{k},y}| \end{pmatrix} e^{-i(N\omega_0 t + S_{\mathrm{dyn}})}. \tag{3.7}$$

We are mainly concerned with the expression form of even-order harmonics (*N*=2*n*, *n* is an integer), the above equation rewritten as

$$\begin{aligned} \begin{pmatrix} J_{\mathrm{er}}^{x} \\ J_{\mathrm{er}}^{\mathrm{y}} \end{pmatrix} &= g_{\boldsymbol{\kappa},0} \begin{pmatrix} \left(e^{-i(\gamma_{\mathrm{B},y}^{+} + \alpha_{\mathrm{DP}}^{+})} - e^{i(\gamma_{\mathrm{B},y}^{-} + \alpha_{\mathrm{DP}}^{-})}\right) |\boldsymbol{d}_{\mathrm{cv}}^{\boldsymbol{k},x}| \\ \left(e^{-i\gamma_{\mathrm{B},y}^{+}} - e^{i\gamma_{\mathrm{B},y}^{-}}\right) |\boldsymbol{d}_{\mathrm{cv}}^{\boldsymbol{k},y}| \end{pmatrix} e^{-i(N\omega_0 t - S_1)} \\ &= g_{\boldsymbol{\kappa},0} \begin{pmatrix} \left(e^{-i\left(\bar{\gamma}_{\mathrm{B},y} + \Delta\gamma_{\mathrm{B},y} + \bar{\alpha}_{\mathrm{DP}} + \delta\alpha_{\mathrm{DP}}\right)} - e^{i\left(\bar{\gamma}_{B,y} - \Delta\gamma_{B,y} + \bar{\alpha}_{DP} - \delta\alpha_{DP}\right)}\right) |\boldsymbol{d}_{\mathrm{cv}}^{\boldsymbol{k},x}| \\ \left(e^{-i\left(\bar{\gamma}_{B,y} + \Delta\gamma_{B,y}\right)} - e^{i\left(\bar{\gamma}_{B,y} - \Delta\gamma_{B,y}\right)}\right) |\boldsymbol{d}_{\mathrm{cv}}^{\boldsymbol{k},y}| \end{pmatrix} e^{-i(N\omega_0 t + S_{\mathrm{dyn}})} \\ &= 2g_{\boldsymbol{\kappa},0} \begin{pmatrix} \sin\left(\bar{\gamma}_{\mathrm{B},y} + \bar{\alpha}_{\mathrm{DP}}\right) |\boldsymbol{d}_{\mathrm{cv}}^{\boldsymbol{k},x}| e^{-i\delta\alpha_{DP}} \\ \sin\left(\bar{\gamma}_{\mathrm{B},y}\right) |\boldsymbol{d}_{\mathrm{cv}}^{\boldsymbol{k},y}| \end{pmatrix} e^{-i(N\omega_0 t + S_{\mathrm{dyn}} + \Delta\gamma_{\mathrm{B},y})}. \end{aligned} \tag{3.8}$$

According to the dipole radiation formula, the expression for the harmonic electric field component is thus

$$\begin{aligned} \begin{pmatrix} E_{\mathrm{even}}^{x} \\ E_{\mathrm{even}}^{y} \end{pmatrix} &= i2N\omega_0 g_{\boldsymbol{\kappa},0} \begin{pmatrix} \sin\left(\bar{\gamma}_{\mathrm{B},y} + \bar{\alpha}_{\mathrm{DP}}\right) |\boldsymbol{d}_{\mathrm{cv}}^{\boldsymbol{k},x}| e^{-i\delta\alpha_{\mathrm{DP}}} \\ \sin\left(\bar{\gamma}_{\mathrm{B},y}\right) |\boldsymbol{d}_{\mathrm{cv}}^{\boldsymbol{k},y}| \end{pmatrix} e^{-i(N\omega_0 t + S_{\mathrm{dyn}} + \Delta\gamma_{\mathrm{B},y})} \\ &= 2N\omega_0 g_{\boldsymbol{\kappa},0} \begin{pmatrix} \sin\left(\bar{\gamma}_{\mathrm{B},y} + \bar{\alpha}_{\mathrm{DP}}\right) |\boldsymbol{d}_{\mathrm{cv}}^{\boldsymbol{k},x}| e^{-i\delta\alpha_{\mathrm{DP}}} \\ \sin\left(\bar{\gamma}_{\mathrm{B},y}\right) |\boldsymbol{d}_{\mathrm{cv}}^{\boldsymbol{k},y}| \end{pmatrix} e^{-i\left(N\omega_0 t + S_{\mathrm{dyn}} + \Delta\gamma_{\mathrm{B},y} + \frac{\pi}{2}\right)}. \end{aligned} \tag{3.9}$$

We further simplify the equation as

$$\begin{pmatrix} E_{\text{even}}^{x} \\ E_{\text{even}}^{y} \end{pmatrix} = \begin{pmatrix} r_x e^{-i\delta\alpha_{\text{DP}}} & 0 \\ 0 & r_y \end{pmatrix} \begin{pmatrix} a_x \\ a_y \end{pmatrix}, \tag{3.10}$$

where, $r_x = \sin(\bar{\gamma}_{\text{B},y} + \bar{\alpha}_{DP})$, $r_y = \sin(\bar{\gamma}_{\text{B},y})$, harmonic amplitudes are given as $a_x = \tilde{g}|\boldsymbol{d}_{\text{cv}}^{\boldsymbol{k},x}|$ and $a_y = \tilde{g}|\boldsymbol{d}_{\text{cv}}^{\boldsymbol{k},y}|$, $\tilde{g} = 2N\omega_0 g_{\boldsymbol{\kappa},0} e^{-i\left(N\omega_0 t + S_{\text{dyn}} + \Delta\gamma_{\text{B},y} + \frac{\pi}{2}\right)} = 2N\omega_0 |\boldsymbol{d}_{\text{cv}}^{\boldsymbol{\kappa}_t}| \boldsymbol{F}(t) e^{-i\left(N\omega_0 t + S_{\text{dyn}} + \Delta\gamma_{\text{B},y} + \frac{\pi}{2}\right)}$ and $a_x/a_y = |\boldsymbol{d}_{\text{cv}}^{\boldsymbol{k},x}|/|\boldsymbol{d}_{\text{cv}}^{\boldsymbol{k},y}|$. Clearly, the amplitude of the harmonic component is directly proportional to the dipole momentum dipole moment magnitudes during both excitation and recombination processes, as well as to the field strength of the driving pulse. The 4×4 matrix appearing on the right-hand side of the equation is coincides the Jones matrix representation of a phase retarder. The phase retardance is rely on the difference of the transition dipole phase $\delta\alpha_{\text{DP}}$.

We then apply spatial transformation to the even-order harmonics. Using mirror symmetry and order-3 rotational symmetry, the orthogonal-component expressions for the harmonic electric field are obtained

$$\begin{pmatrix} E_x \\ E_y \end{pmatrix} = M_\theta \begin{pmatrix} r_x e^{-i\delta\alpha_{\text{DP}}} & 0 \\ 0 & r_y \end{pmatrix} \begin{pmatrix} a_x \\ a_y \end{pmatrix}. \tag{3.11}$$

Here, $M_\theta = \begin{pmatrix} \sin^2 3\theta & -\sin 3\theta \cos 3\theta \\ -\sin 3\theta \cos 3\theta & \cos^2 3\theta \end{pmatrix}$ describes the spatial symmetry operation, 3θ means the mirror plane rotates every 120°.

3.3 Harmonic components of two-color pulse as the driver

The asymmetric light field interacts with symmetry-broken states, inducing quantum phase modulation as a function of the two-color phase delay. The classical action can be decomposed as

$$S(t',t,\boldsymbol{k}) \approx S_{\text{dyn}}(\boldsymbol{\kappa}_{t',t}^{\text{o}}) + \gamma_{\text{B}}(\boldsymbol{\kappa}_{t',t}^{\text{o}}) + \sigma_{S_{\text{dyn}}} + \sigma_{\gamma_{\text{B}}}, \tag{3.12}$$

where the $\boldsymbol{\kappa}_{t',t}^{\text{o}} = \boldsymbol{k} + \boldsymbol{A}_\omega(t') - \boldsymbol{A}_\omega(t)$ is the crystal momentum as a function of fundamental field only. Crucially, the perturbative SH field does not alter the birth and recombination times of e-h pairs, but predominantly governs the evolution of e-h trajectories through phase modification. In this case, $\sigma_{S_{\text{dyn}}}$ and $\sigma_{\gamma_{\text{B}}}$ correspond to phase correction terms of the dynamic phase and geometric phase modified by the SH field respectively, which are explicitly expressed as

$$\sigma_{S_{\text{dyn}}} = \int_{t'}^{t} \Delta v_{\text{g}} \left(\boldsymbol{\kappa}_{t,\tau}^{\text{o}}\right) A_{2\omega} \cos(2\omega\tau + \phi_{2\omega}) \mathrm{d}\tau, \tag{3.13}$$

which scales linearly with the band's group velocity Δv_{g} and $A_{2\omega}(t)$ is the vector potential of SH field,

$$\sigma_{\gamma_{\text{B}}} = \int_{t'}^{t} \Delta\mathcal{A}(\boldsymbol{\kappa}_{t,\tau}^{\text{o}}) F_{2\omega} \sin(2\omega\tau + \phi_{2\omega}) \mathrm{d}\tau, \tag{3.14}$$

which describes a Berry phase acquired along the SH field perturbed evolution path, with the second term on the right-hand side becomes negligible under weak perturbation conditions. So, the geometric phase correction is proportional to the SH field and the combined Berry connection.

Since the weak SH field polarized along the pump polarization, it primarily modified the phase accumulation along the pump polarization while left the dynamics in perpendicular direction unaffected, as the measurements in Ref. [2]. For positive or negative half-cycles of the fundamental field, the SH field oscillations are the same. The expression of the interband current with the SH field correction takes the form of

$$\begin{pmatrix} J_{\text{er}}^{x} \\ J_{\text{er}}^{\text{y}} \end{pmatrix} = g_{\boldsymbol{\kappa},0} \begin{pmatrix} \left(e^{-i\gamma_{\text{B},x}^{+}} - e^{-iN\pi} \cdot e^{i\gamma_{\text{B},x}^{-}}\right) |\boldsymbol{d}_{\text{cv}}^{\boldsymbol{k},x}| \\ \left(e^{-i\left(\gamma_{\text{B},y}^{+} + \sigma_{S_{\text{dyn}}} + \delta\gamma_{\text{B}}\right)} - e^{-iN\pi} \cdot e^{i\left(\gamma_{\text{B},y}^{+} + \sigma_{S_{\text{dyn}}} - \delta\gamma_{\text{B}}\right)}\right) |\boldsymbol{d}_{\text{cv}}^{\boldsymbol{k},y}| \end{pmatrix} e^{-i(N\omega_0 t - S_{\text{dyn}})}, \tag{3.15}$$

in which the phase correction terms induced by SH field only appear in the y-component. After similar derivation procedure as above, we then get

$$\begin{pmatrix} J_{\text{er}}^{x} \\ J_{\text{er}}^{\text{y}} \end{pmatrix} = 2g_{\boldsymbol{\kappa},0} \begin{pmatrix} \sin\left(\overline{\gamma}_{\text{B},y} + \overline{\alpha}_{\text{DP}}\right) |\boldsymbol{d}_{\text{cv}}^{\boldsymbol{k},x}| e^{-i\,\delta\alpha_{DP}} \\ \sin\left(\overline{\gamma}_{\text{B},y} + \sigma_{S_{\text{dyn}}}\right) |\boldsymbol{d}_{\text{cv}}^{\boldsymbol{k},y}| e^{-i\sigma_{\gamma_{\text{B}}}} \end{pmatrix} e^{-i(N\omega_0 t - S_{\text{dyn}} + \Delta\gamma_{\text{B},y})}. \tag{3.16}$$

The harmonic radiation arising from dipole processes $E_{\mathrm{HHG}}(N\omega_0) = iN\omega_0 J(N\omega_0)$

Thus, we can write out the harmonic components

$$\begin{pmatrix} E_{\mathrm{even}}^{x} \\ E_{\mathrm{even}}^{y} \end{pmatrix} = 2N\omega_0 g_{\boldsymbol{\kappa},0} \begin{pmatrix} \sin(\bar{\gamma}_{\mathrm{B},y} + \bar{\alpha}_{\mathrm{DP}}) |\boldsymbol{d}_{\mathrm{cv}}^{\boldsymbol{k},x}| e^{-i\delta\alpha_{\mathrm{DP}}} \\ \sin(\bar{\gamma}_{\mathrm{B},y} + \sigma_{S_{\mathrm{dyn}}}) |\boldsymbol{d}_{\mathrm{cv}}^{\boldsymbol{k},y}| e^{-i\sigma_{\gamma_{\mathrm{B}}}} \end{pmatrix} e^{-i\left(N\omega_0 t + S_{\mathrm{dyn}} + \Delta\gamma_{B,y} + \frac{\pi}{2}\right)}, \tag{3.17}$$

and further simplify to

$$\begin{pmatrix} E_{\mathrm{even}}^{x} \\ E_{\mathrm{even}}^{y} \end{pmatrix} = \begin{pmatrix} r_x e^{-i\delta\alpha_{\mathrm{DP}}} & 0 \\ 0 & r_y' e^{-i\sigma_{\gamma_{\mathrm{B}}}} \end{pmatrix} \begin{pmatrix} a_x \\ a_y \end{pmatrix}. \tag{3.18}$$

Here, $r_y' = \sin(\bar{\gamma}_{\mathrm{B},y})$ and σ_{γ_B} is the modified phase retardance amplitude and phase, respectively.

Through spatial operation, the harmonic electric field has the form of

$$\begin{pmatrix} E_x \\ E_y \end{pmatrix} = \left[M_\theta \begin{pmatrix} r_x e^{-i\delta\alpha_{\mathrm{DP}}} & 0 \\ 0 & r_y e^{-i\sigma_{\gamma_B}} \end{pmatrix} + \begin{pmatrix} 0 \\ \Delta r_y e^{-i\sigma_{\gamma_B}} \end{pmatrix} \right] \begin{pmatrix} a_x \\ a_y \end{pmatrix}, \tag{3.19}$$

where, $\Delta r_y = \cos(\bar{\gamma}_{\mathrm{B},y}) \sin(\sigma_{S_{\mathrm{dyn}}})$ describes the y-component contribution of the SH field.

If the pump field polarized along the ΓK direction, matrix reads $M_\theta = \begin{pmatrix} 1 & 0 \\ 0 & 0 \end{pmatrix}$, and the harmonic fields are given as

$$\begin{cases} E_{\mathrm{even}}^{x} = r_x a_x e^{-i\delta\alpha} \\ E_{\mathrm{even}}^{y} = \Delta r_y a_y e^{-i\sigma_{\gamma_B}} \end{cases}. \tag{3.20}$$

Obviously, the harmonic amplitude of the y-component is proportional to the SH field, since $E_{\mathrm{even}}^{y} \propto \sin(\sigma_{S_{\mathrm{dyn}}}) \sim \sigma_{S_{\mathrm{dyn}}} \sim F_{2\omega}$, $\sigma_{S_{\mathrm{dyn}}}$ is small. The harmonic intensity therefore scales as $I_{\mathrm{even}}^{y} \propto F_{2\omega}^{2}$.

Reference

1. Ishizaka, K. et al. Giant Rashba-type spin splitting in bulk BiTeI. *Nat. Mater.* **10**, 521–526 (2011).

2. Bai, Y. et al. Probing Berry phase effect in topological surface states. *Phys. Rev. Lett.* **133**, 243801 (2024).
3. Baykusheva, D. et al. Strong-field physics in three-dimensional topological insulators. *Phys. Rev. A* **103**, 023101 (2021).
4. Uzan-Narovlansky, A. J. et al. Observation of interband Berry phase in laser-driven crystals. *Nature* **626**, 66–71 (2024).
5. Xiao, D., Chang, M.-C. & Niu, Q. Berry phase effects on electronic properties. *Rev. Mod. Phys.* **82**, 1959–2007 (2010).
6. Li, J. *et al.* Phase invariance of the semiconductor Bloch equations. *Phys. Rev. A* **100**, 043404 (2019).
7. Yue, L. & Gaarde, M. B. Imperfect recollisions in high-harmonic generation in solids. *Phys. Rev. Lett.* **124**, 153204 (2020).
8. Qian, C. *et al.* Role of shift vector in high-harmonic generation from noncentrosymmetric topological insulators under strong laser fields. *Phys. Rev. X* **12**, 021030 (2022).
9. Alon, O. E., Averbukh, V. & Moiseyev, N. Selection rules for the high harmonic generation spectra. *Phys. Rev. Lett.* **80**, 3743–3746 (1998).
10. Neufeld, O., Podolsky, D. & Cohen, O. Floquet group theory and its application to selection rules in harmonic generation. *Nat. Commun.* **10**, 1–9 (2019).
11. Tzur, M. E., Neufeld, O., Bordo, E. et al. Selection rules in symmetry-broken systems by symmetries in synthetic dimensions. *Nat. Commun.* **13**, 1312 (2022).
12. Qian, C., Jiang, S. C., Wu, T. et al. Theory of solid-state harmonic generation governed by crystal symmetry. *Phys. Rev. B* **109**, 205401 (2024).